Thermoelectric properties of In0.2Co4Sb12 skutterudites with embedded PbTe or ZnO nanoparticles

Caroline Chubilleau, Bertrand Lenoir, Christophe Candolfi, Philippe Masschelein, Anne Dauscher, Emmanuel Guilmeau, Claude Godart

Thermoelectric properties of $In_{0.2}Co_4Sb_{12}$ skutterudites with embedded PbTe or ZnO nanoparticles

C. Chubilleau[1], B. Lenoir[1], C. Candolfi[1], P. Masschelein[1], A. Dauscher[1,*], E. Guilmeau[2], C. Godart[3]

[1] Université de Lorraine, CNRS (UMR 7198), Institut Jean Lamour, Parc de Saurupt, 54011 Nancy, France

[2] Laboratoire CRISMAT, UMR 6508, 6 boulevard Maréchal Juin, 14050 Caen Cedex

[3] ICMPE-CMTR, CNRS-UMR 7182, 2-8 rue H. Dunant, 94320 Thiais, France

* Corresponding author : anne.dauscher@univ-lorraine.fr, tel : +33 383 584 170, fax : +33 383 584 347

Abstract

Transport properties of the skutterudite compound $In_{0.2}Co_4Sb_{12}$ containing ZnO or PbTe nano-sized particles (2-12 wt.%) were investigated by means of electrical resistivity, thermopower and thermal conductivity between 5 and 800 K. The composite powders were prepared by freeze-drying the nanoparticles with micron-sized $In_{0.2}Co_4Sb_{12}$ powders. Densification was achieved by spark plasma sintering. All composites were characterized by X-ray powder diffraction and scanning electron microscopy. All the transport coefficients show similar temperature dependences suggesting little influence of the nature, semiconducting or insulating, of the nanoparticles. Both the electrical and the thermal conductivities decrease with increasing the PbTe or ZnO content. The impact of ZnO and PbTe on the thermal conductivity was modelled based on the Debye model taking into account a relaxation time constant reflecting phonon scattering by spherical nanoparticles. A maximum dimensionless figure of merit *ZT* of 1.05 at 700 K was achieved in a sample containing 2 wt.% ZnO, a value quite similar to that of the reference $In_{0.2}Co_4Sb_{12}$ compound.

Keywords: A: thermoelectric materials, C: electrical transport, C: thermal transport, C: microstructure

1. Introduction

The development of novel highly-efficient thermoelectric materials for solid-state energy conversion - refrigeration and electrical generation from waste heat - is currently at the core of worldwide investigations. The efficiency of a thermoelectric material is governed by the dimensionless figure of merit ZT defined as $ZT = \frac{S^2 T}{\rho(\kappa_e + \kappa_l)}$ where S is the Seebeck coefficient (or thermopower), ρ is the electrical resistivity and T is the absolute temperature [1]. In this equation, the total thermal conductivity κ is the sum of the electrical κ_e and the lattice contributions κ_l. ZT improvement is thus obtained by simultaneously achieving low thermal conductivity, low electrical resistivity and high thermopower. The main obstacle to overcome is related to the fact that the thermopower is inversely related to the electrical conductivity according to the Boltzmann transport equation and, as a result, maximisation of one cannot be achieved without minimisation of the other [2].

Skutterudites such as $CoSb_3$ are considered as thermoelectric materials of great interest due to their good electrical properties. Nevertheless, their too high thermal conductivity constitutes a limiting factor to achieve ZT values beyond unity [3-4]. Among the strategies used to optimize their thermoelectric properties, atomic substitutions on the Co or Sb sites and/or single or even multiple-filling were extensively studied [5, and refs therein]. More recently, bulk nanostructuring, associated or not with the two previous means, has also steered their performance towards significant improvement. Indeed, this interesting way allows increasing phonon scattering on the numerous interfaces thereby lowering the thermal conductivity. Different kinds of nanostructured compounds have been on focus: consolidated nanopowders [6-10], quenched-in nanostructures [5,11-14], mixed nano-micron sized powders [15-28] or in-situ formed nanostructures [29-33].

In prior studies, we reported the effect on thermoelectric properties of semiconducting PbTe [25,26] or insulating ZnO [27,28] nano-sized particles embedded in a micron-sized $CoSb_3$ matrix. While both types of inclusions were found beneficial near room temperature, their influence at higher

temperatures was more elusive. This last result was due to a change in conduction type for PbTe (from *p* to *n* in the absence and presence of PbTe, respectively) and to large agglomeration of the nanoparticles at the grain boundaries for ZnO.

Here, we extend this approach to an optimized single-filled skutterudite $In_{0.2}Co_4Sb_{12}$ (*ZT* value of 1.05 at 700 K [34]) and investigate the influence on the transport properties of the presence of PbTe and ZnO nanoparticles. The paper is organized as follows. After presenting the experimental details, we discuss the results of a theoretical model developed with the aim of studying the influence of nanoparticles on the thermal transport. The analysis of the structural and chemical characterizations is followed by the results of the electrical and thermal properties and eventually, the dimensionless thermoelectric figure of merit.

2. Experimental procedures

2.1. Synthesis of the materials

Polycrystalline samples of nominal composition $In_{0.4}Co_4Sb_{12}$ were prepared by a combination of melting and solid-state reactions [35-36]. Stoechiometric amounts of high-purity In shots (99.99%), Sb shots (99.999%), and Ni-free Co (99.998%) powders were loaded into quartz ampoules in an argon-atmosphere glovebox. The tubes were sealed under He/H_2 atmosphere, placed in a vertical rocking furnace and heated up to 650°C at a rate of 1°C/min. After a dwell time of 84 h at this temperature, the ampoules were finally quenched in a room-temperature water bath. The obtained ingots were then ground in an agate mortar into fine powders (<100 μm) that were cold-pressed into pellets. To ensure a good chemical homogeneity of the skutterudite phase, the pellets were annealed in a quartz ampoule sealed under He/H_2 atmosphere at 650°C for 120 h. Prior to the densification process, the annealed pellets were powdered again (<50 μm). The same batch was used to prepare both series of composites (ZnO and PbTe).

The ZnO nanoparticles were purchased from Alfa Aesar with a size of about 100 nm as measured by transmission electron microscopy. The PbTe nanoparticles were prepared by laser fragmentation in water from PbTe micron-sized particles according to the method described in Ref. 37. The mean size of the spherically-shaped nanoparticles is about 6 nm in diameter. The x wt% PbTe and ZnO ($0 \leq x \leq 12$) composites were prepared via a liquid route from a stoichiometric mixture of micron-sized skutterudite powders and PbTe or ZnO nanoparticles. Water was used as the dispersing medium in the presence of PbTe while a methanol/hexane (3:1) mixture at 0.025 M was used with ZnO [27,28]. The as-dispersed compounds in the liquid (20 min in an ultrasonic bath) were then immediately immerged in liquid nitrogen and dried by freeze-drying during 12 hours (FTS-EZ585 system, 17 mTorr, - 80°C). Finally, the composite powders were densified by spark plasma sintering (SPS Dr Sinter 515S) in graphite dies (10.4 mm in diameter) at 600°C during 6 min under 50 MPa. The relative densities of the specimens (Table 1) were finally evaluated from their dry mass and geometrical dimensions with respect to their theoretical densities, d_{th}, calculated using Eq. (2) which takes into account the theoretical densities (d_i) and the mass fraction (x) of each species ($d_{CoSb3} = 7.64$; $d_{ZnO} = 5.67$; $d_{PbTe} = 8.27$):

$$d_{th} = \frac{1}{x/d_{inclusion} + (1-x)/d_{matrix}} \quad (2)$$

2.2 Materials characterization and transport properties measurements

Structural characterizations were performed by powder X-ray diffraction (PXRD) on a Bruker D8 Advance diffractometer using Co $K\alpha_1$ radiation in a 2θ-range of 25°- 60°. The PXRD patterns were analyzed by the Rietveld method implemented in the Fullprof software [38] using the structural parameters of $CoSb_3$ as a starting model. The microstructure of the samples was characterized by scanning electron microscopy (SEM) on a Philips FEG XL 30. Electron probe microanalysis (EPMA) was carried out to check the chemical homogeneity and composition of all the samples obtained after

the SPS treatment. The actual compositions of the skutterudite matrix were $In_{0.20}Co_4Sb_{11.79}$ and $In_{0.20}Co_4Sb_{11.86}$ for the ZnO- and PbTe-containing samples and did not show significant variations with the amount of nanoparticles introduced (these chemical formulae were normalized to four cobalt atoms). Hereafter, the samples will be labelled using this actual composition.

Low-temperature thermoelectric properties (2-300 K) were measured simultaneously using a physical properties measurement system (PPMS, Quantum Design) with the thermal transport option TTO under zero magnetic field. The bar-shaped samples (of typical dimensions 2.5×2.5×9 mm^3) were cut perpendicularly to the press direction. The copper bars used as thermal and electrical contacts were attached onto the samples using BiSn braze. Hall coefficient measurements were conducted on the same samples between 5-300 K by sweeping the magnetic field between -3 and +3T with the ACT option of the PPMS. A five-probe method was used to carry out these measurements.

High-temperature electrical resistivity and thermopower were simultaneously measured between 300 and 700 K using an ULVAC-ZEM3 apparatus. The total thermal conductivity was calculated from the thermal diffusivity D measured between 300 and 700 K with the laser flash technique (NETZSCH LFA 427), the specific heat C_p (NETZSCH DSC 404 F3 Pegasus), and the density d using Eq.(3).

$$\kappa = D \times C_p \times d \qquad (3)$$

3. Results and discussion

3.1. Theoretical model

In order to get insights into the influence of both the nanoparticles size and the volume fraction on the thermal transport, we tried to model the lattice thermal conductivity of the In-filled skutterudite taking into account the presence of nanoparticles. Within the Debye model, κ_l is written as

$$\kappa_r = \frac{k_B}{2\pi^2 v}\left(\frac{k_B}{\hbar}\right)^3 T^3 \int_0^{\theta_D/T} \tau(x,T)\frac{x^4 e^x}{\left(e^x-1\right)^2}dx \quad (4)$$

where k_B is the Boltzmann constant, v is the sound velocity, $\hbar$ is the reduced Planck constant, $\tau(x,T)$ is the relaxation time of phonons and $x = \hbar\omega / k_B T$ is a dimensionless parameter with ω the phonon pulsation. If we adopt the Matthiessen rule, $\tau(x,T)$ is the sum of several mechanisms assumed to be independent from each other:

$$\tau^{-1} = \frac{v}{L} + A\omega^4 + B\omega^2 T e^{-\theta_D/3T} + \frac{C\omega^2}{(\omega_0^2-\omega^2)^2} \quad (5)$$

In Eq.(5), the first term represents phonon scattering by grain boundaries with L the mean grain size, the second term is related to point defect scattering (Rayleigh diffusion), the third term is associated to phonon-phonon scattering (Umklapp processes) and the last term stands for the interaction between the vibrational normal modes of the structure and the modes of the In atoms considered as localized (Einstein oscillators). In this last term, ω_0 is the characteristic vibrational pulsation of the In atoms. The presence of nanoparticles is expected to disrupt the heat-carrying phonons giving rise to an additional relaxation time. We followed here the model developed by Mingo *et al*. [39] who assumed spherical nanoparticles distributed homogeneously in the skutterudite matrix. This model includes an additional relaxation time written as

$$\tau_{np}^{-1} = v\left(\sigma_s^{-1} + \sigma_l^{-1}\right)^{-1} d_n \quad (6)$$

where d_n is the density of nanoparticles (in m^{-3}) and σ_s and σ_l are the short- and long-wavelength scattering cross sections, respectively. This formula is based on a Matthiessen-like relation between the

short and long-wavelength diffusive regimes of phonons scattered by the nanoparticles. d_n is related to the volume fraction and the radius R of the nanoparticles by $d_n = f / (4\pi R^3/3)$. The two scattering cross sections are expressed as

$$\sigma_s = 2\pi R^2 \tag{7}$$

$$\sigma_l = \pi R^2 \frac{4}{9}\left(\frac{\Delta D}{D}\right)^2\left(\frac{\omega R}{v}\right)^4 \tag{8}$$

where ΔD and D are the difference in density between the matrix and the nanoparticles and the density of the matrix, respectively. The set of Eq.(4), (5) and (6) contains no adjustable parameters so that the relaxation time of phonon diffusion by nanoparticles can be evaluated numerically as a function of both the volume fraction and the radius. We applied this approach to the In-filled and In-free nanocomposites (Refs. 25 and 27) to determine the role played by both a homogeneous distribution of nanoparticles and In atoms on κ_l. As a first step, the lattice thermal conductivity data of the nanoparticle-free compounds were fitted according to Eq.(4) with L, A, B, C and ω_0 as free parameters and using v = 2967 m.s^{-1} measured by a conventional pulse-echo method. The results obtained for $CoSb_3$ and $In_{0.2}Co_4Sb_{12}$ are listed in Table 1. Assuming that the presence of nanoparticles has a negligible influence on these values, we used them to compute the lattice thermal conductivity temperature dependences of the composites. The influence of the nanoparticle sizes was first investigated keeping constant the volume fraction to 1.9 % (corresponding to 2 wt% of PbTe). Several interesting results emerge from these calculations compiled in Figure 1 for $CoSb_3$ and $In_{0.2}Co_4Sb_{12}$ containing either ZnO or PbTe nanoparticles. In the case of the parent compound $CoSb_3$, an optimum size of the nanoparticles that minimizes κ_l exists (Figs 1a and 1b). These sizes fall in the 6-8 and 2-4 nm ranges for PbTe and ZnO, respectively, resulting in respective decreases of the dielectric maximum of up to 66 and 73%. In addition, below 10 nm, the oxide nanoparticles have a stronger impact due to a more pronounced density difference. Upon

introducing In in the skutterudite matrix, the optima sizes are shifted to 14 and 6 nm for PbTe and ZnO, respectively (Figs 1c and 1d). This model further shows that nanoparticles primarily affect the low-temperature region as it is seen from the strong decrease in the dielectric maximum of the $\kappa_l(T)$ curves. At 300 K, their influence is lessened though still discernable. Yet, because this model is strictly applicable up to the Debye temperature (around 320 K in the present case), it is not possible to determine whether or not the observed effect would vanish at higher temperatures.

Figure 2 shows κ_l as a function of the nanoparticle size for the four series of composites at 300 K with a volume fraction of 1.9%. This plot clearly emphasizes the role played by the nanoparticle's size on the reduction of the lattice thermal conductivity. Surprisingly, the relative decrease in κ_l appears significantly more pronounced in In-filled samples than in $CoSb_3$ as shown in Figures 2b and 2d. One may expect a weaker impact of the nanoparticles on κ_l due to the much lower values in the In-filled compounds with respect to $CoSb_3$. This rather counterintuitive result may nevertheless be explained by the mass fluctuations induced by the In atoms. Meisner *et al*. [40] demonstrated that partially-filled skutterudites can be seen as a solid solution of unfilled and filled skutterudite phases. Because the long-wavelength phonons are the main heat carriers in alloys, their mean free path exceeds the typical distance between nanoparticles. The probability for these phonons to be scattered will be therefore higher in partially filled compounds than in unfilled compounds thereby explaining the stronger reduction seen in In-filled compounds.

Finally, we adjusted the parameters of the model (volume fraction and grain size) to those of our PbTe/ZnO $In_{0.2}Co_4Sb_{12}$ samples to try to predict their thermal behavior. The results are plotted in Figures 2e and 2f. From these plots, it is clear that the higher the volume fraction is, the higher the decrease in the lattice thermal conductivity. We also note that the dielectric maximum is shifted to higher temperatures. While for the PbTe nanocomposites the reduction amounts to 50% at 300 K, the reduction observed in the ZnO composites is lower (20%) even though still noticeable.

3.2. Phase and microstructure

For the PbTe-$In_{0.2}Co_4Sb_{12}$ series, the relative densities remain higher than 95%, except for the highest PbTe content (12%, see Table 2) for which it decreases to 90%. In the ZnO counterparts, the relative densities decrease down to 90% with increasing the ZnO content. For a similar weight ratio, the volume ratio will be higher for ZnO than for PbTe suggesting only little difference in density between the two series of samples. Surprisingly, the presence of indium seems to limit the densification retardation observed for the similarly prepared ZnO-$CoSb_3$ series studied in ref. [27,28]. Higher porosity induced by the presence of nanoparticles was already underlined in thermoelectric composites such as ZrO_2/$CoSb_3$ [17], SiC/Bi_2Te_3 [41] or ceramics [42]. Among the possible mechanisms that were invoked to explain this result [43], mechanical stresses induced by the presence of rigid inclusions seem to be more likely in the present case. However, the non-homogeneous distribution of the nanoparticles (see below) may also play a role.

The PXRD patterns of the different densified samples (Figure 3) show similar features. In addition to the main peaks that can be indexed to the cubic skutterudite structure, some additional peaks indicate the presence of a small amount of secondary phases (mainly InSb). The intensity of the diffraction peaks of PbTe (Figure 3a) and ZnO (Figure 3b) increases with their nominal fraction *x*, suggesting that the inclusions are not finely dispersed into the skutterudite matrix. This behaviour is similar to that observed in In-free composites PbTe-$CoSb_3$ and ZnO-$CoSb_3$ [25-28]. Interestingly, in the case of the 12wt%-ZnO specimen, a diffraction peak located around 29° was identified as being $Zn_3CoInSbO_8$ (JCPDS: 04-008-3988), evidencing that a reaction occurred between the matrix and the nanoparticles during the SPS process. Shi *et al.* [44] have also observed the formation of a Ba_6C_{60} phase in their study on C_{60}/$Ba_{0.44}Co_4Sb_{12}$ composites. However, the presence of this phase was found to strongly modify both the chemical composition and the unit cell parameter of the skutterudite structure.

In our case, no variations in the lattice parameter could be observed regardless of the ZnO mass fraction in the sample (Table 1). The same conclusion can be drawn for the PbTe series.

SEM images were collected in the backscattered electron mode (BSE) to determine the distribution of the phases in the different samples (Figure 4). PbTe agglomerates at grain boundaries (Figures 4b to 4d) as already seen in the PbTe-$CoSb_3$ series [25,26]. X-ray mapping (Figures 5a to 5f) further corroborates this conclusion and reveals that InSb is also located at the grain boundaries. Li *et al*. [31] as well as Mallik *et al*. [33] have already observed that InSb phases are formed in indium filled skutterudites and located preferentially at the grain boundaries. The grain size of the skutterudite matrix is around 3-5 μm, fairly lower than the grain size suggested by the location of either PbTe or InSb. The presence of ZnO in the skutterudite matrix results in an important loss of density that is obviously seen on the images (Figures 4e to 4h) as pores around the grains. Likewise the PbTe series, the ZnO particles are agglomerated at the grain boundaries and form large areas whose size can exceeds 50 μm (mottled black and white zones in Figure 4f). This kind of microstructures, where micron-sized clusters of nanoparticles with irregular shape surround the matrix grains, is not restricted to the present samples and was already observed in composites such as for example $Yb_2O_3/Yb_{0.25}Co_4Sb_{12}$ [16], ZrO_2/ZrNiSn [45], C_{60}/Bi_2Te_3 [46], $C_{60}/R_xCo_4Sb_{12}$ [47]. Observations on fractured samples revealed the tendency of the powder-like aspect of the oxide to agglomerate. The ultrasound mixing method employed here is thus not efficient enough to break and disperse the ZnO agglomerates contained in the commercial powder. As a result, this leads to the presence of very porous and large clusters of oxide that are not densified by the sintering temperature used (the sintering temperature of ZnO is near 1300 °C).

3.3. Electrical and galvanomagnetic properties

The temperature dependences of the thermopower S and the Hall coefficient R_H are shown in Figure 6 and in the inset, respectively. Both S and R_H are negative over the entire temperature range investigated for both series indicative of a dominant electron-like character. The presence of nanoparticles thus does not alter the behavior of the parent $In_{0.2}Co_4Sb_{12}$ skutterudite which originates from the electron transfer from In to the host framework. The results relative to $In_{0.2}Co_4Sb_{12}$ are in very good agreement with those obtained in prior studies [34,47,48]. Between 2 and 300 K, both series exhibit a quasi-linear temperature dependence consistent with that of a degenerate electron gas. At higher temperatures, the samples experience minority carrier effects that lower the absolute S values. A slight difference with the PbTe content is observed in the PbTe-$In_{0.2}Co_4Sb_{12}$ series. Even though the presence of In mainly drives the transport properties, a minute amount of Te substituting Sb likely explains the observed trend. The temperature dependence of S in the ZnO-$In_{0.2}Co_4Sb_{12}$ series is composition-independent in stark contrast with the behaviour observed in the ZnO-$CoSb_3$ series. In the In-free series, the influence of ZnO was attributed to the presence of potential barriers which no longer seem to be at play upon inserting In. This suggests that both the electron concentration and their scattering mechanisms should be independent with the ZnO concentration.

The electron concentrations n and Hall mobilities $\mu_H = R_H/\rho$ of the two series of composites are plotted as a function of temperature in Figures 7 and 8. The room temperature values are listed in Table 1. Both series show similar variations in n with temperature. The values range from 1×10^{20} up to 2×10^{20} cm^{-3} at 300 K and decrease only slightly with temperature as expected in degenerate semiconductors. This behavior is typical of n-type partially filled skutterudites [3,49]. Noteworthy, neither the presence of PbTe nor the presence of ZnO influences the electron concentration in agreement with the thermopower data. The Hall mobility of the $In_{0.2}Co_4Sb_{12}$ sample is in agreement with literature data [47,50]. The presence of PbTe, ZnO and pores does not modify the scattering mechanisms of electrons

i.e. neutral impurities scattering below 80 K and acoustic phonons scattering above this temperature. The influence of nanoparticles and pores is however detrimental to the μ_H values which decrease by a factor of 5 (1.4) at 5 K and 2 (1.2) at 300 K between the reference sample and the 12wt%-PbTe specimen (8wt%-ZnO).

Combining the galvanomagnetic and thermopower data, the reduced effective mass of electrons m^*/m_0 (m_0 is the bare electron mass) were estimated at 300 K (Table 1) assuming a single-parabolic-band model described in detail elsewhere [34]. For both series of composites, m^* remain close to that of the reference sample, implying no obvious change in the electronic band structure. Figure 9 displays a comparison of the evolution of m^*/m_0 as a function of the carrier concentration n in our materials and for n-type skutterudites $R_xCo_4Sb_{12}$ (R = Ba [51,52] – Tl [53] – Nd [54] – Ce [55] – La [56] – Ca [5,49]). As can be seen, our results match the general trend of n-type partially-filled skutterudites. The slight increase in m^*/m_0 with n might be related to the presence of several conduction bands at the Γ and H points of the Brillouin zone, a feature not included in the present model [34].

The temperature dependence of the electrical resistivity of the In partially-filled skutterudites follows an almost linear trend typical of degenerate semiconductors (Figure 10). If the insertion of In strongly reduce ρ with respect to $CoSb_3$ (by a factor of 6 at 300 K), the addition of either PbTe or ZnO has less incidence on the ρ (T) data (Figures 10a and 10b). Yet, ρ drops sharply below 7.2 K in the PbTe-$In_{0.2}Co_4Sb_{12}$ composites (Figure 10a). This temperature corresponds to the superconducting transition temperature of Pb indicating that some PbTe nanoparticles decompose into elemental Pb and Te. While Pb does not substitute for Co nor for Sb, Te does substitute for Sb. This result further corroborates the trend observed in the *S(T)* data suggesting that a minute amount of Te substitute for Sb. Between 7.2 and 50 K, ρ decreases slowly in the PbTe-based composites while the ZnO analogues shows a different behaviour (Figure 10b). Above 50 K, both series show trends similar to the reference $In_{0.2}Co_4Sb_{12}$ skutterudite, with a monotonically increase in ρ with temperature. The ρ values tend to

increase with the amount of inclusions due to the observed degradation of the Hall carrier mobility, a behavior well documented for various nanocomposite systems [17,35,57-61].

3.4. Thermal transport

The temperature dependence of the total thermal conductivity for all samples are depicted in Figures 11a and 11b. Near room temperature some deviations between the low and high temperature measurements are evidenced. This is attributed to the different methods used to probe the thermal conductivity. In the low temperature range, thermal losses by radiation are present. They start to play a role for T > 150 K and increase with T according to a T^3 law. As a result, the thermal conductivity is overestimated when 150 < T ≤ 300 K. The electronic contribution κ_e was estimated using the Wiedemann-Franz law ($\kappa_e = LT/\rho$ where L is the Lorenz number taken to the value of a degenerate electron gas $L_0 = 2.44\times10^{-8}$ V^2K^{-2}). The ambipolar contribution dominating above 600 K was not taken into account in the following analysis. The lattice thermal conductivity κ_l was then deduced from $\kappa = \kappa_e + \kappa_l$. The two contributions κ_e and κ_l are plotted in Figures 11c and 11d for the PbTe and ZnO series, respectively. In $In_{0.2}Co_4Sb_{12}$, the dielectric maximum is divided by eight with respect to $CoSb_3$ and the room-temperature value is reduced by 70%. This two main features originate from the presence of In in the cage-like structure of $CoSb_3$. The dispersion of ZnO leads to a slight decrease in κ_l below 300 K with the amount of nanoparticles up to 8%. The increase observed for 12% is most likely due to the lower density of this sample. Above 300 K, the presence of nanoparticles has only little influence leading to quasi-constant κ_l values. No clear correlation between the fraction of PbTe nanoparticles and κ_l is evidenced by our data. This is presumably due to varying amount of Te substituting for Sb in the skutterudite matrix. The exact influence of the nanoparticles is nevertheless difficult to unveil since In, the porosity and the nanoparticles that tend to agglomerate play a role in determining κ_l. To lessen the impact of the former, we corrected the total κ values following Eq.(4). [62]

$$\kappa_{100\%} = \frac{2\kappa}{3d-1} \quad (9)$$

The results are reported in Figure 12 for both series of samples, showing only a weak decrease in the total thermal conductivity in fully dense samples. Because of the tendency of the nanoparticles to agglomerate, the comparison of the theoretical model with our experimental data in the 5 – 300 K temperature range is quite delicate. According to the model (see Figure 2), increasing the diameter of the particles decreases the corresponding scattering rate of phonons. For diameters higher than 300 nm, only a modest reduction in the lattice thermal conductivity may be expected. This expectation is in qualitatively good agreement with the results shown in Figure 12. Nevertheless, it appears difficult to draw a final conclusion due to the complex microstructure of our samples that inevitably plays a role in determining the thermal transport.

3.5. Dimensionless thermoelectric figure of merit ZT

The calculated dimensionless figure of merit *ZT* of the different composites are presented in Figure 13 as a function of temperature. Compared to $CoSb_3$, the introduction of In leads to a maximum *ZT* of 1.0 at 700 K, due to higher thermopower and lower thermal conductivity values. Both series of composites exhibit temperature dependences quite similar to the reference skutterudite. The values are however systematically lower in the whole temperature range. An exception to this trend is observed in the 2wt%-PbTe and 2wt%-ZnO samples that exhibit similar values up to 500 K. These results differ from those obtained in the ZnO-$CoSb_3$ series for which, a slight increase in *ZT* was observed at low ZnO contents [27]. At higher temperatures, the *ZT* of the PbTe series seems more detrimentally affected than that of the ZnO series, perhaps due to the minute amount of Te substituting for Sb as previously observed in the PbTe-$CoSb_3$ series [25]. Nevertheless, the *ZT* values of the ZnO series range between 0.78 and 1.03 at 700 K.

4. Conclusion

We presented the transport properties of PbTe-$In_{0.2}Co_4Sb_{12}$ and ZnO-$In_{0.2}Co_4Sb_{12}$ nanocomposites between 2 and 800 K. SEM experiments revealed the tendency of the nanoparticles to agglomerate at the grain boundaries by forming large clusters. As a result, this non-homogeneously dispersion leads to a loss of density. The transport properties of both series of sample show similar temperature dependences suggesting that the nature of the nanoparticles (insulating versus semiconducting) does not play a significant role in the present case. The *n*-type electrical conduction of the parent $In_{0.2}Co_4Sb_{12}$ skutterudite is preserved upon introducing nanoparticles. While this conclusion holds true for the scattering mechanisms of electrons, this is no longer the case for the electron mobilities that tend to decrease with increasing the nanoparticle content. The analysis of the thermal properties revealed to be quite complex because of the presence of In, porosity and nano-inclusions that may all be a diffusion source of phonons. Generally, as expected, a reduction in the thermal conductivity was observed for both types of nanoparticles. The main aspects of the influence of nanoparticles on κ_l was captured by a model that explicitly takes into account phonon scattering by spherically-shaped particles. Despite this reduction and contrarily to results observed in *e.g.* Ba-filled skutterrudites with Ag nanoparticles [24], the high *ZT* values of the $In_{0.2}Co_4Sb_{12}$ matrix (*ZT* > 1) is not improved by the presence of nanoinclusions.

Acknowledgments

The authors acknowledge support from the European Network of Excellence CMA 'Complex Metallic Alloys'.

References

[1] D.M. Rowe, Thermoelectrics Handbook: Macro to Nano, CRC Taylor & Francis Group, Boca Raton, 2005.

[2] R.W. Ure, R.R. Heikes, Thermoelectricity : Science and Engineering, Interscience Publisher, 1961.

[3] C. Uher, Skutterudites: prospective novel thermoelectrics, in T. Tritt (Ed.), Semiconductors and Semimetals, Academic Press, San Diego, 2001, Vol. 69, p. 139.

[4] B.C. Sales, D. Mandrus, R.K. Williams, Science 272 (1996) 1325.

[5] C. Uher, Recent advances in the development of efficient n-type skutteudites, in D. M. Rowe (Ed.), Thermoelectrics and its energy harvesting: modules, systems, and applications in thermoelectrics, CRC Press, 2012, Chap. 10.

[6] M.S. Toprak, C. Stiewe, D. Platzek, S. Williams, L. Bertini, E. Müller, C. Gatti, Y. Zhang, D.M. Rowe, M. Muhammed, Adv. Func. Mater. 14 (2004) 1189.

[7] P.N. Alboni, X. Ji, J. He, N. Gothard, J. Hubbard, T.M. Tritt, J. Elec. Mater. 36 (2007) 711.

[8] J.L. Mi, X.B. Zhao, T.J. Zhu, J.P. Tu, Mater. Let. 62 (2008) 2363.

[9] L. Zhang**,** A. Grytsiv, M. Kerberc, P. Rogl, E. Bauer, M.J. Zehetbauer, J. Wosik, G.E. Nauer, J. All. Comp. 481 (2009) 106.

[10] E. Alleno, M. Gaborit, V. Ohorodniichuk, B. Lenoir, O. Rouleau, J. Elec. Mater. 42 (2013) 1835.

[11] X. Tang, W. Xie, H. Li, B. Du, Q. Zhang, T.M. Tritt, C. Uher, High performance nanostructured thermoelectric materials prepared by melt-spinning and spark plasma sintering, in D. M. Rowe (Ed.), Thermoelectrics and its energy harvesting: Materials, preparation, and characterization in thermoelectrics , CRC Press, 2012, Chap. 16.

[12] H. Li, X. Tang, X. Su, Q. Zhang, C. Uher, J. Phys. D: Appl. Phys. 42 (2009) 145409.

[13] H. Li, X. Tang, Q. Zhang, C. Uher, Appl. Phys. Lett. 93 (2008) 252109.

[14] J.R. Salvador, R.A. Waldo, C.A. Wong, M. Tessema, D.N. Brown, D.J. Miller, H. Wang, A.A. Wereszczak, W. Cai, Mater. Sci. Engin. B 178 (2013) 1087.

[15] S. Katsuyama, Y. Kanayama, M. Ito, K. Majima, H. Nagai, J. Appl. Phys. 88 (2000) 3484-3489.

[16] X.Y. Zhao, X. Shi, L.D. Chen, W.Q. Zhang, S.Q. Bai, Y.Z. Pei, X.Y. Li, T. Goto, Appl. Phys. Lett. 89 (2006) 092121.

[17] Z. He, C. Stiewe, D. Platzek, G. Karpinski, E. Müller, S. Li, M. Toprak, M. Muhammed, Nanotechnol. 18 (2007) 1; J. Appl. Phys. 101 (2007) 043707.

[18] J.L. Mi, T.J. Zhu, X.B. Zhao, J. Ma, J. Appl. Phys. 101 (2007) 054314; J.L. Mi, X.B. Zhao, T.J. Zhu, J.P. Tu, Appl. Phys. Lett. 92 (2008) 029905.

[19] E. Alleno, L. Chen, C. Chubilleau, B. Lenoir, O. Rouleau, M.F. Trichet, B. Villeroy, J. Elec. Mater. 39 (2010) 1966.

[20] H.Q. Liu, G. Zhou, F.X. Hao, Y.J. Gu, X.B. Zhao, J. Inorg. Organomet. Polym. 21 (2011) 862.

[21] C. Zhou, J. Sakamoto, D. Morelli, X. Zhou, G. Wang, C. Uher, J. Appl. Phys. 109 (2011) 063722.

[22] B. Duan, P. Zhai, P. Wen, S. Zhang, L. Liua, Q. Zhang, Scripta Mater. 67 (2012) 372.

[23] S. Katsuyama, F. Maezawa, T. Tanaka, J. Phys.: Conf. Series 379 (2012) 012004.

[24] X. Zhou, G. Wang, L. Zhang, H. Chi, X. Su, J. Sakamoto, C. Uher, J. Mater. Chem. 22 (2012) 2958.

[25] C. Chubilleau, B. Lenoir, A. Dauscher, C. Godart, Intermetallics 22 (2012) 47.

[26] C. Chubilleau, B. Lenoir, P. Masschelein, A. Dauscher, C. Candolfi, E. Guilmeau, C. Godart, J. Mater. Sci. 48 (2013) 2761.

[27] C. Chubilleau, B. Lenoir, P. Masschelein, A. Dauscher, C. Candolfi, E. Guilmeau, C. Godart, J. All. Comp. 554 (2013) 340.

[28] C. Chubilleau, B. Lenoir, P. Masschelein, A. Dauscher, C. Godart, J. Elec. Mater. 41 (2012) 1181.

[29] S. Katsuyama, M. Watanabe, M. Kuroki, T. Maehata, M. Ito, J. Appl. Phys. 93 (2003) 2758.

[30] Z. Xiong, L. Xi, J. Ding, X. Chen, X. Huang, H. Gu, L. Chen, W. Zhang, J. Mater. Res. 26 (2011) 1848.

[31] H. Li, X. Tang, Q. Zhang, C. Uher, Appl. Phys. Lett. 94 (2009) 102114.

[32] J. Eilertsen, S. Rouvimov, M.A. Subramanian, Acta Mater. 60 (2012) 2178.

[33] R.C. Mallik, C. Stiewe, G. Karpinsk, R. Hassdorf R, E. Müller, J. Elec. Mater. 38 (2009) 1337.

[34] J. Leszczynski, V. Da Ros, B. Lenoir, A. Dauscher, C. Candolfi, P. Masschelein, J. Hejtmanek, K. Kutorasinski, J. Tobola, R.I. Smith, C. Stiewe, E. Müller, Accepted in J. Phys. D: Appl. Phys. (2013).

[35] V. Da Ros, J. Leszczynski, B. Lenoir, A. Dauscher, C. Candolfi, P. Masschelein, C. Bellouard, C. Stiewe, E. Müller, J. Hejtmanek, Proc. Mater. Res. Soc. Symp., (2008) 1044-U1005-1006.

[36] J. Leszczynski, V. Da Ros, B. Lenoir, A. Dauscher, C. Candolfi, P. Masschelein, C. Bellouard, C. Stiewe, E. Müller, J. Hejtmanek, Proc. 6th European Conf. Thermoelectrics, Paris, (2008) O20.

[37] C. Chubilleau, B. Lenoir, S. Migot, A. Dauscher, J. Coll. Interf. Sci. 357 (2011) 13.

[38] J. Rodríguez-Carvajal, J. Phys. B: Cond. Matter 192 (1993) 55.

[39] N. Mingo, D. Hauser, N.P. Kobayashi, M. Plissonnier, A. Shakouri, Nano Lett. 9 (2009) 711.

[40] G.P. Meisner, D.T. Morelli, S. Hu, J. Yang, C. Uher, Phys. Rev Lett. 80 (1998) 3551.

[41] L.D. Zhao, B.P. Zhang, J.F. Li, M. Zhou, W.S. Liu, J. Liu, J. All. Comp. 455 (2008) 259.

[42] Y. Nakada, T. Kimura, J. Amer. Ceram. Soc. 80 (1997) 401.

[43] C.L. Fan, M.N. Rahaman, J. Amer. Ceram. Soc. 75 (1992) 2056.

[44] X. Shi, L.D. Chen, S.Q. Bai, X.Y. Huang, X.Y. Zhao, Q. Yao, C. Uher, J. Appl. Phys. 102 (2007) 103709.

[45] X.Y. Huang, Z. Xu, L.D. Chen, Solid State Comm. 130 (2004) 181.

[46] N. Gothard, J.E. Spowart, T.M. Tritt, Phys. Stat. Sol. (A): Applic. Mater. 207 (2010) 157.

[47] R.C. Mallik, J.Y. Jung, S.C. Ur, I.H. Kim, Metals Mater. Internat. 14 (2008) 223.

[48] T. He, J. Chen, H.D. Rosenfeld, M.A. Subramanian, Chem. Mater. 18 (2006) 759.

[49] M. Puyet, B. Lenoir, A. Dauscher, P. Pécheur, C. Bellouard, J. Tobola, J. Hejtmanek, Phys. Rev. B – Cond. Matter Mater. Phys. 73 (2006) 035126.

[50] J. Leszczynski, A. Dauscher, P. Masschelein, B. Lenoir, J. Elec. Mater. 39 (2010) 1764.

[51] L.D. Chen, T. Kawahara, X.F. Tang, T. Goto, T. Hirai, J.S. Dyck, W. Chen, C. Uher, J. Appl. Phys. 90 (2001) 1864.

[52] J.S. Dyck, W. Chen, C. Uher, L.D. Chen, X. Tang, T. Hirai, J. Appl. Phys. 91 (2002) 3698.

[53] B.C. Sales, B.C. Chakoumakos, D. Mandrus, Phys. Rev. B-Cond. Matter Mater. Phys., 61 (2000) 2475.

[54] V.L. Kuznetsov, L.A. Kuznetsova, D.M. Rowe, J. Phys. Cond. Mat. 15 (2003) 5035.

[55] D.T. Morelli, G.P. Meisner, B. Chen, S. Hu, C. Uher, Phys. Rev. B – Cond. Matter Mater. Phys. 56 (1997) 7376.

[56] G.S. Nolas, J.L. Cohn, G.A. Slack, Phys. Rev. B – Cond. Matter Mater. Phys. 58 (1998) 164.

[57] Z. Xiong, X. Chen, X. Zhao, S. Bai, X. Huang, L. Chen, Solid State Sci. 11 (2009) 1612.

[58] P.N. Alboni, X. Ji, J. He, N. Gothard, T.M. Tritt, J. Appl. Phys. 103 (2008) 113707.

[59] M. Ito, T. Tada, S. Katsuyama, J. All. Comp. 350 (2003) 296.

[60] M. Ito, T. Tanaka, S. Hara, J. Appl. Phys. 95 (2004) 6209.

[61] L.D. Chen, X.Y. Huang, M. Zhou, X. Shi, W.B. Zhang, J. Appl. Phys. 99 (2006) 064305.

[62] R. Landauer, Electrical conductivity in inhomogeneous media, in: J.C. Garland, D.B. Tanner, Eds, Electrical Transport and Optical Properties of Inhomogeneous Media, American Institute of Physics: New York, 1978, pp 2.

Table 1: Values of the fitting parameters used to describe the lattice thermal conductivity of the $CoSb_3$ and $In_{0.2}Co_4Sb_{12}$ skutterudites.

Material	L (μm)	A (10^{-43} s^3)	B (10^{-18} $s.K^{-1}$)	C (10^{33} s^{-3})	ω_0 (THz)
Co_4Sb_{12}	4.4	3.4	3.3	/	/
$In_{0.2}Co_4Sb_{12}$	4.9	137.7	2.8	2.6	6.2

Table 2: Theoretical density d_{th}, relative density d_{rel}, and cell parameter a (evaluated by Rietveld refinements of the PXRD diagrams) of the PbTe-$In_{0.2}Co_4Sb_{12}$ and ZnO-$In_{0.2}Co_4Sb_{12}$ composites. The carrier concentrations n, Hall mobilities μ_H, thermopower S were measured at 300 K. The reduced effective masses of electrons m^*/m_0 were estimated at 300 K.

Composite	d_{th}	d_{rel} (%)	a (Å)	n (cm^{-3})	μ_H ($cm^2V^{-1}s^{-1}$)	S (μVK^{-1})	m^*/m_0
$In_{0.2}Co_4Sb_{12}$	7.69	98	9.0565(2)	$1.87x10^{20}$	49	-145	2.6
+ 2% PbTe	7.65	96	9.0563(2)	$1.86x10^{20}$	37	-159	3.0
+ 8% PbTe	7.69	96	9.0559(2)	$1.19x10^{20}$	48	-162	2.3
+ 12% PbTe	7.71	90	9.0565(2)	$1.35x10^{20}$	29	-162	2.5
+ 2% ZnO	7.59	98	9.0567(2)	$1.80x10^{20}$	49	-143	2.6
+ 4% ZnO	7.54	94	9.0562(2)	$1.32x10^{20}$	51	-144	2.1
+ 8% ZnO	7.43	89	9.0565(2)	$1.10x10^{20}$	41	-143	1.8
+ 12% ZnO	7.33	89	9.0564(2)	$1.54x10^{20}$	34	-146	2.3

Figure caption

Figure 1: Modeling of the temperature dependences of the lattice thermal conductivity for a) PbTe-$CoSb_3$, b) ZnO-$CoSb_3$, c) PbTe-$In_{0.2}Co_4Sb_{12}$, d) ZnO-$In_{0.2}Co_4Sb_{12}$ composites for various PbTe or ZnO particle diameters, assuming an homogeneous dispersion of 1.9 volume ratio of nanoparticles in the skutterudite matrix.

Figure 2: Theoretical influence of the PbTe or ZnO particles size on the reduction in the lattice thermal conductivity of $CoSb_3$ and $In_{0.2}Co_4Sb_{12}$ skutterudites. a) PbTe or ZnO-$CoSb_3$ composites (actual values), b) PbTe or ZnO-CoSb3 composites (relative values to $CoSb_3$), c) PbTe or ZnO-$In_{0.2}Co_4Sb_{12}$ composites (actual values), (d) PbTe or ZnO-$In_{0.2}Co_4Sb_{12}$ composites (relative values to $In_{0.2}Co_4Sb_{12}$). The 1.9 volume fraction of PbTe or ZnO particles are assumed to be homogeneously dispersed in the skutterudite matrix. Theoretical temperature dependences of the lattice thermal conductivity of the $In_{0.2}Co_4Sb_{12}$ compound for different fractions of PbTe (e) and ZnO (f).

Figure 3: XRD patterns of the PbTe- (a) and ZnO-$In_{0.2}Co_4Sb_{12}$ (b) composites. Note the minute amount of secondary phases (Sb, InSb, $CoSb_2$, $Zn_3CoInSbO_8$).

Figure 4: SEM backscattered electron images of a) $In_{0.2}Co_4Sb_{12}$, b-d) PbTe-$In_{0.2}Co_4Sb_{12}$ composites and e-h) ZnO-$In_{0.2}Co_4Sb_{12}$ composites.

Figure 5: BSE images and their corresponding X-ray mapping images for a)-f) 8wt%PbTe-$In_{0.2}Co_4Sb_{12}$ composites and g)-k) 8wt%ZnO-$In_{0.2}Co_4Sb_{12}$ composites.

Figure 6: Temperature dependences of the thermopower S for a) PbTe-$In_{0.2}Co_4Sb_{12}$ composites and b) ZnO-$In_{0.2}Co_4Sb_{12}$ composites. The temperature dependence of the Hall coefficient R_H is shown in the insets.

Figure 7: Temperature dependences of the carrier concentrations n for a) PbTe-$In_{0.2}Co_4Sb_{12}$ composites and b) ZnO-$In_{0.2}Co_4Sb_{12}$ composites.

Figure 8: Temperature dependences of the Hall mobility μ_H for a) PbTe-$In_{0.2}Co_4Sb_{12}$ composites and b) ZnO-$In_{0.2}Co_4Sb_{12}$ composites.

Figure 9: Evolution of the reduced effective mass m^*/m_0 as a function of the carrier concentration for PbTe and ZnO composites. Comparison with n-type $R_xCo_4Sb_{12}$ skutterudites with various filler atoms R.

Figure 10: Temperature dependences of the resistivity ρ for a) PbTe-$In_{0.2}Co_4Sb_{12}$ composites and b) ZnO-$In_{0.2}Co_4Sb_{12}$ composites. The inset highlights the superconducting transition at 7.2 K characteristic of Pb.

Figure 11: Temperature dependences of the total thermal conductivity, κ, for a) PbTe-$In_{0.2}Co_4Sb_{12}$ composites and b) ZnO-$In_{0.2}Co_4Sb_{12}$ composites. Temperature dependences of the electronic $\kappa_{\square}$ (solid lines) and lattice $\kappa_{\square}$ (symbols) thermal contributions for c) PbTe-$In_{0.2}Co_4Sb_{12}$ composites and d) ZnO-$In_{0.2}Co_4Sb_{12}$ composites.

Figure 12: Temperature dependences of the total thermal conductivity corrected from porosity according to Eq. (4) in the 2.4-300 K temperature range for a) PbTe-$In_{0.2}Co_4Sb_{12}$ composites, b) ZnO-$In_{0.2}Co_4Sb_{12}$ composites.

Figure 13: Temperature dependences of the dimensionless figure of merit ZT for a) PbTe-$In_{0.2}Co_4Sb_{12}$ composites and b) ZnO-$In_{0.2}Co_4Sb_{12}$ composites.

Highlights

- Fabrication of nanostructured skutterudites ZnO or PbTe/$In_{0.2}Co_4Sb_{12}$
- Thermal conductivity modeling accounts for experimental results
- Greater lattice thermal conductivity decrease in $In_{0.2}Co_4Sb_{12}$ than in $CoSb_3$
- A max ZT of 1.05 is obtained at 700 K in a 2wt.% ZnO-containing sample

Figure

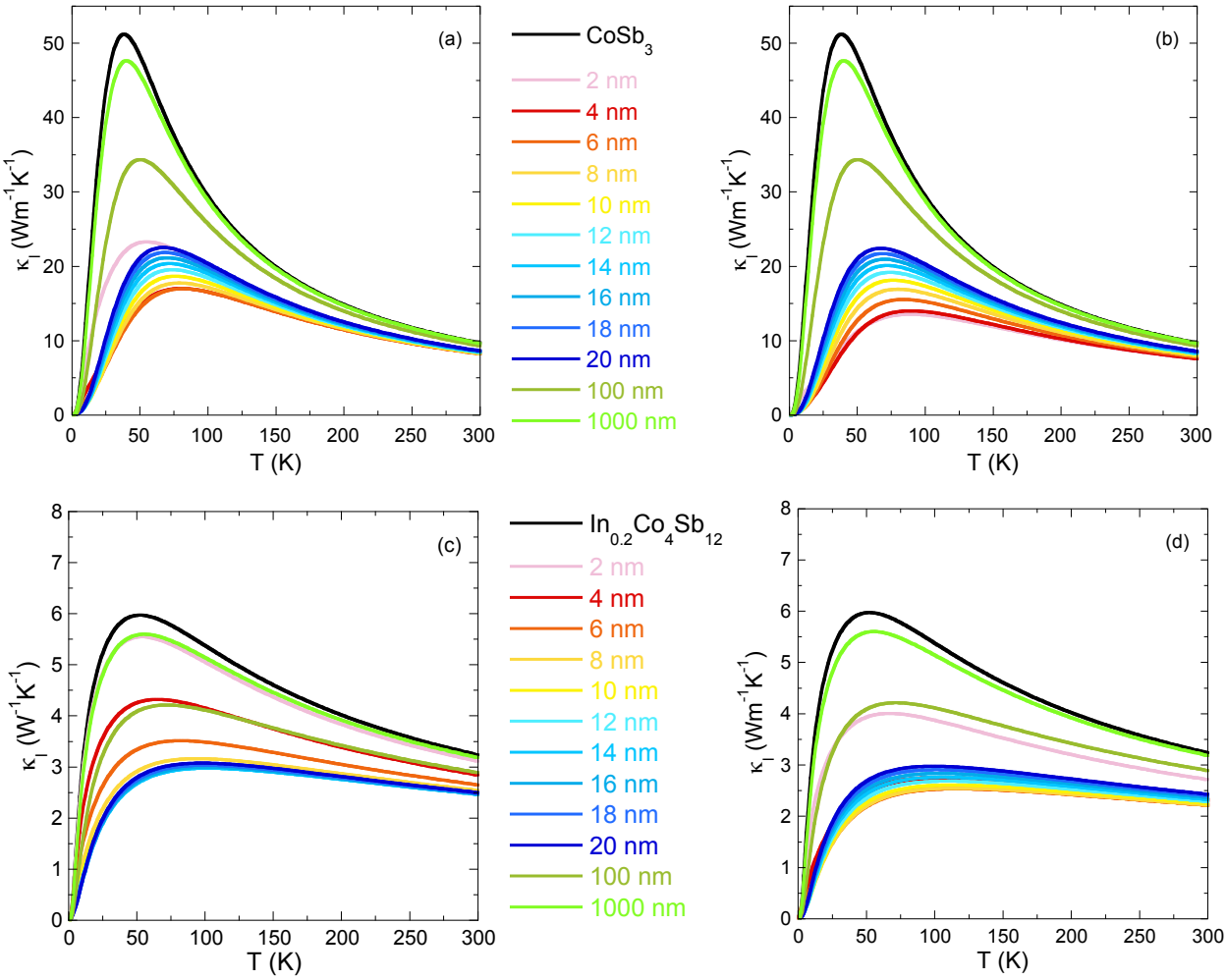
(a)
(b)
(c)
(d)
κ_l (Wm^{-1}K^{-1})
κ_l (W^{-1}K^{-1})
T (K)
CoSb$_3$
In$_{0.2}$Co$_4$Sb$_{12}$
2 nm
4 nm
6 nm
8 nm
10 nm
12 nm
14 nm
16 nm
18 nm
20 nm
100 nm
1000 nm

Figure

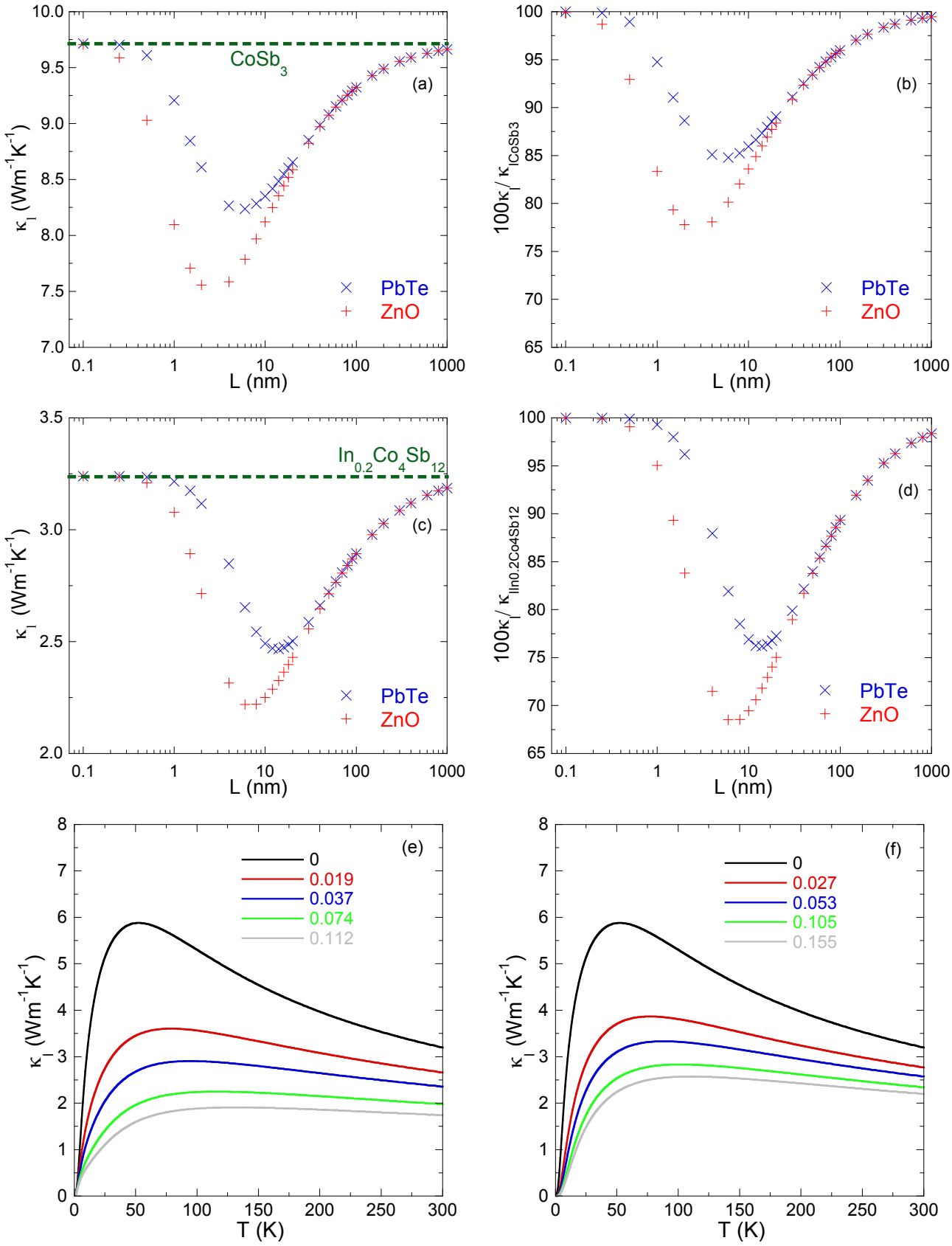
(a)
CoSb3
PbTe
ZnO
κl (Wm-1K-1)
L (nm)
(b)
100κl/ κlCoSb3
(c)
In0.2Co4Sb12
(d)
100κl/ κlIn0.2Co4Sb12
(e)
0
0.019
0.037
0.074
0.112
T (K)
(f)
0
0.027
0.053
0.105
0.155

Figure

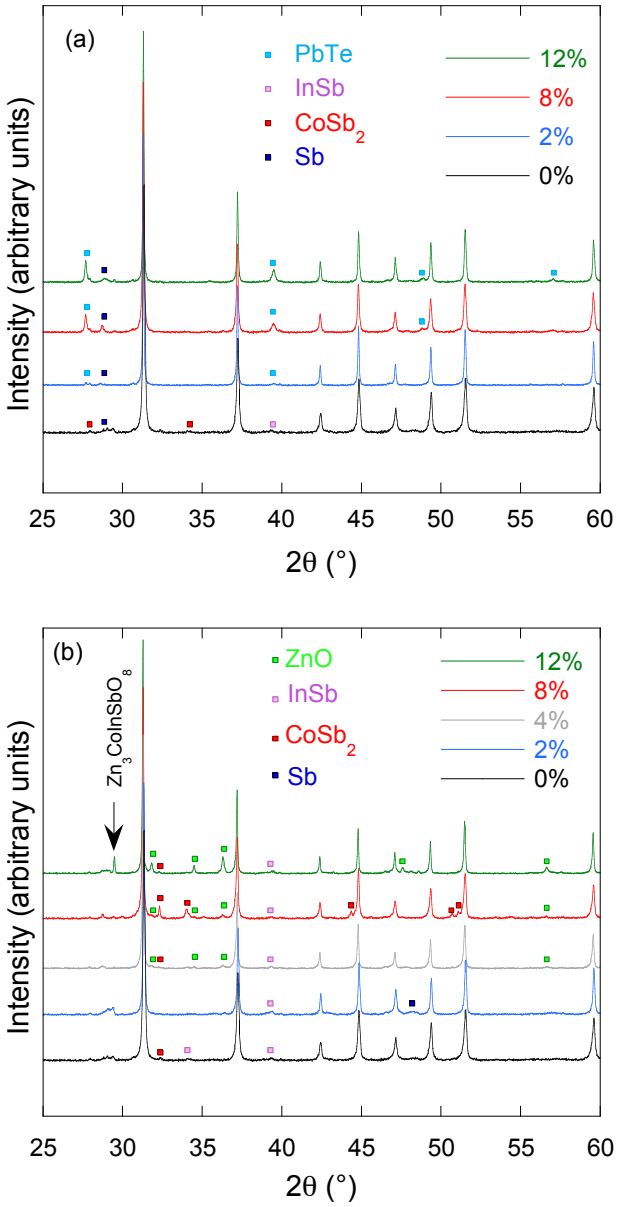
(a)
PbTe
InSb
CoSb2
Sb
12%
8%
2%
0%
Intensity (arbitrary units)
25
30
35
40
45
50
55
60
2θ (°)
(b)
ZnO
InSb
CoSb2
Sb
Zn3CoInSbO8
12%
8%
4%
2%
0%
Intensity (arbitrary units)
25
30
35
40
45
50
55
60
2θ (°)

Figure

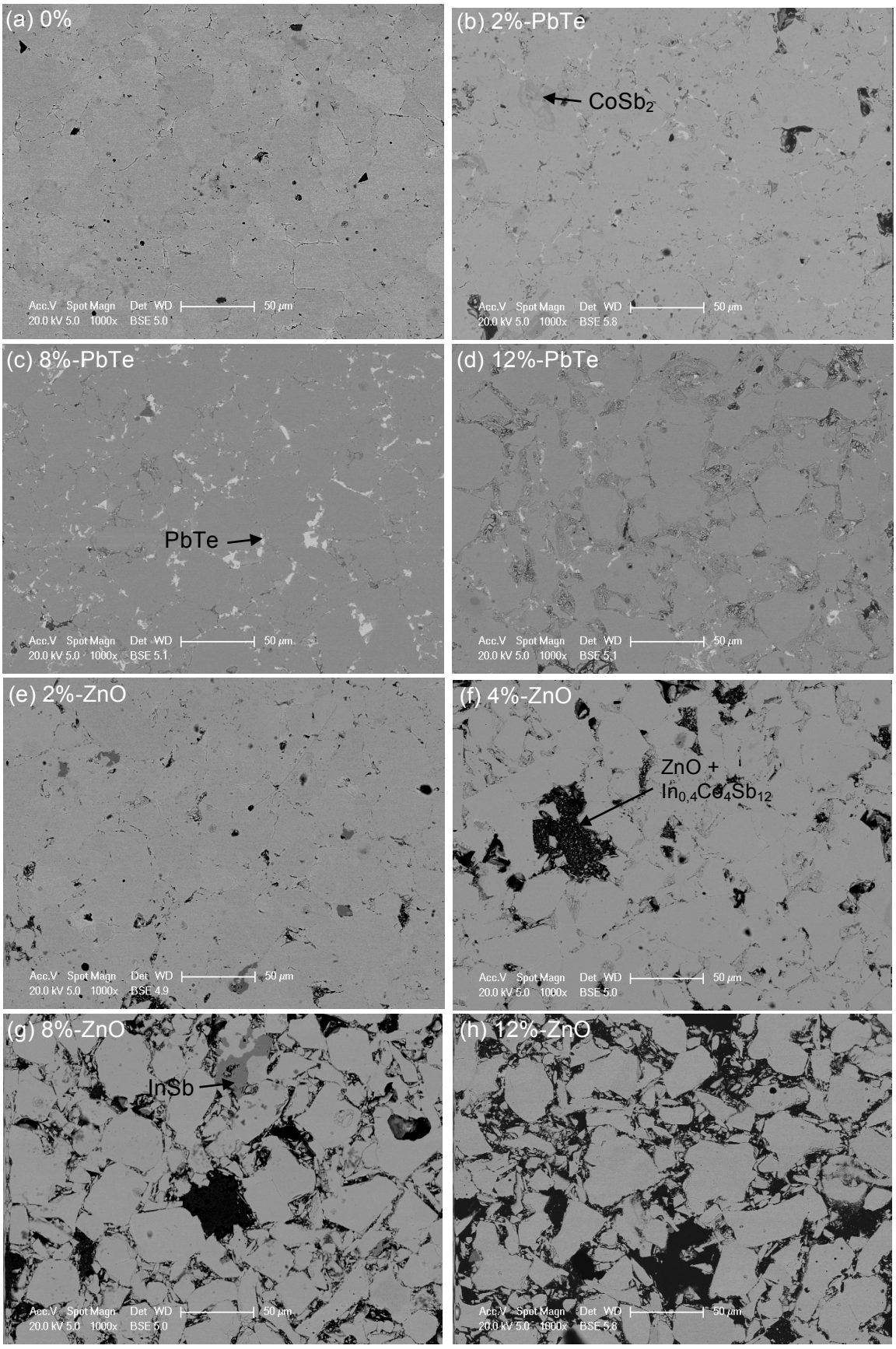
(a) 0%
Acc.V Spot Magn Det WD 50 μm
20.0 kV 5.0 1000x BSE 5.0
(b) 2%-PbTe
CoSb2
Acc.V Spot Magn Det WD 50 μm
20.0 kV 5.0 1000x BSE 5.8
(c) 8%-PbTe
PbTe
Acc.V Spot Magn Det WD 50 μm
20.0 kV 5.0 1000x BSE 5.1
(d) 12%-PbTe
Acc.V Spot Magn Det WD 50 μm
20.0 kV 5.0 1000x BSE 5.1
(e) 2%-ZnO
Acc.V Spot Magn Det WD 50 μm
20.0 kV 5.0 1000x BSE 4.9
(f) 4%-ZnO
ZnO +
In0.4Co4Sb12
Acc.V Spot Magn Det WD 50 μm
20.0 kV 5.0 1000x BSE 5.0
(g) 8%-ZnO
InSb
Acc.V Spot Magn Det WD 50 μm
20.0 kV 5.0 1000x BSE 5.0
(h) 12%-ZnO
Acc.V Spot Magn Det WD 50 μm
20.0 kV 5.0 1000x BSE 5.8

Figure

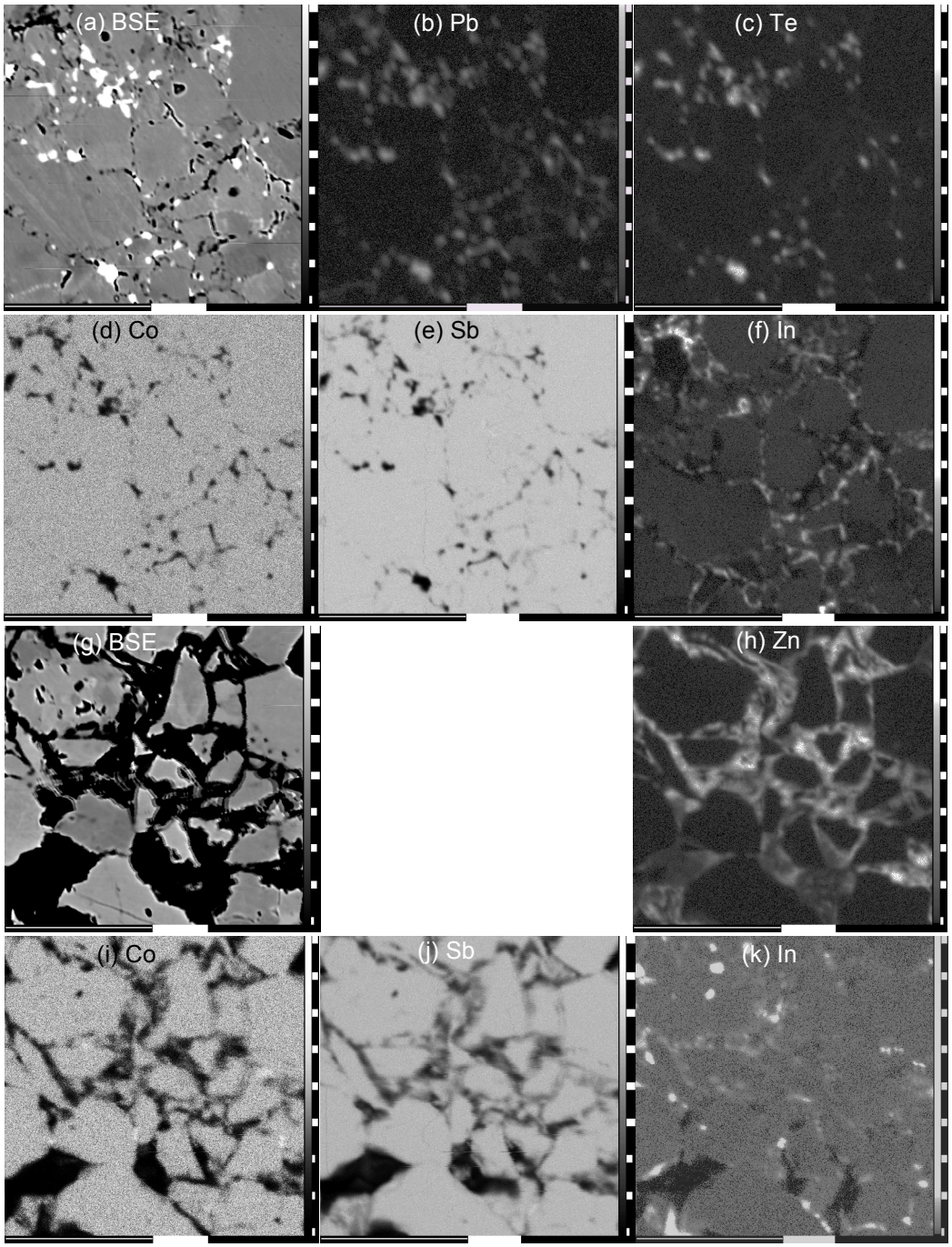

Figure

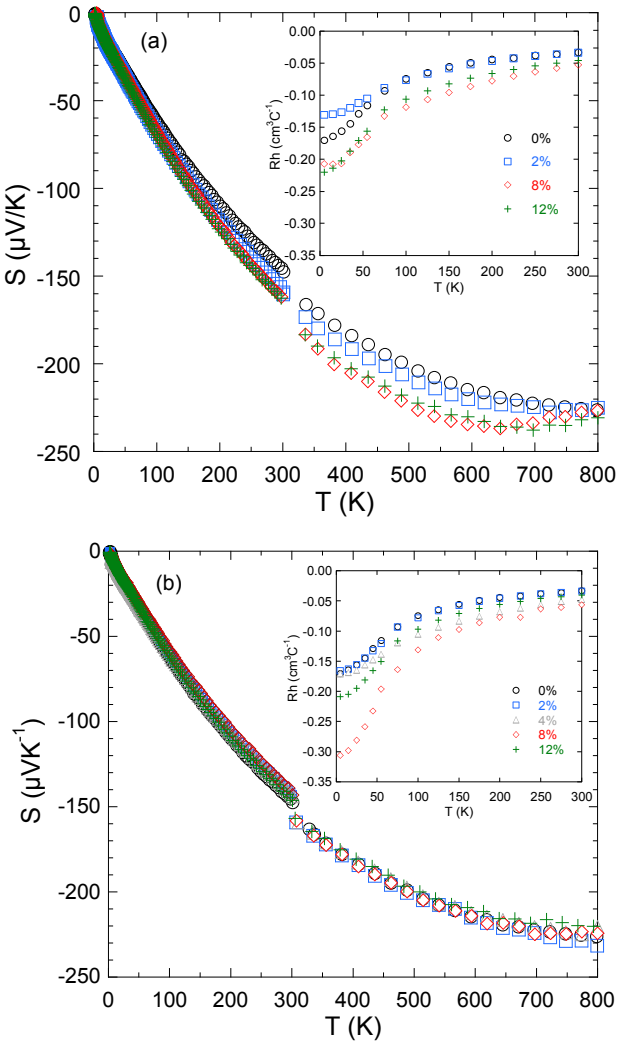

Figure

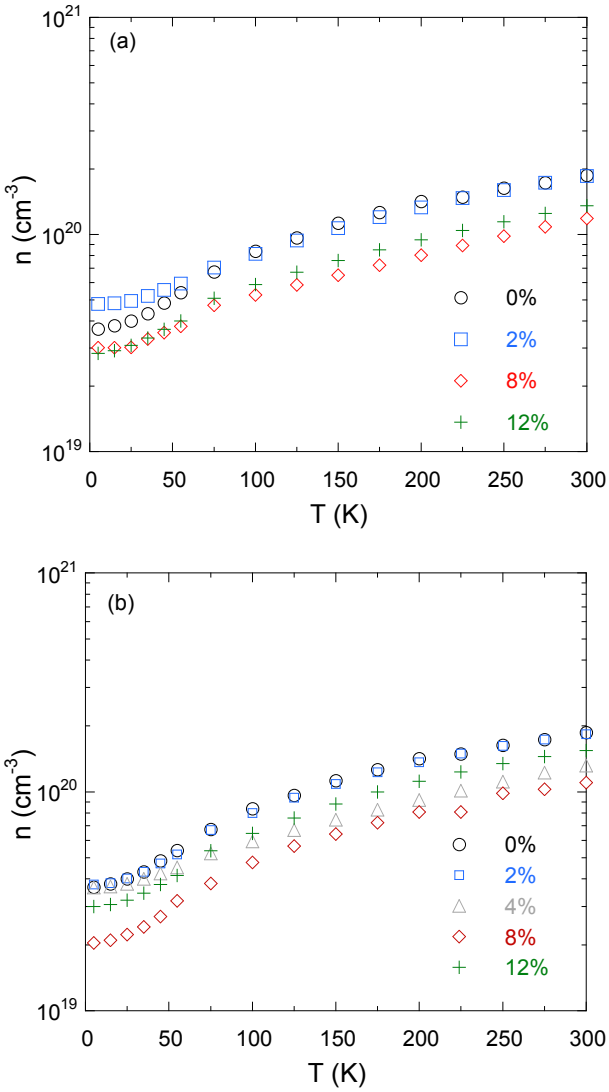
(a)
n (cm^{-3})
10^{21}
10^{20}
10^{19}
0
50
100
150
200
250
300
T (K)
0%
2%
8%
12%
(b)
n (cm^{-3})
10^{21}
10^{20}
10^{19}
0
50
100
150
200
250
300
T (K)
0%
2%
4%
8%
12%

Figure

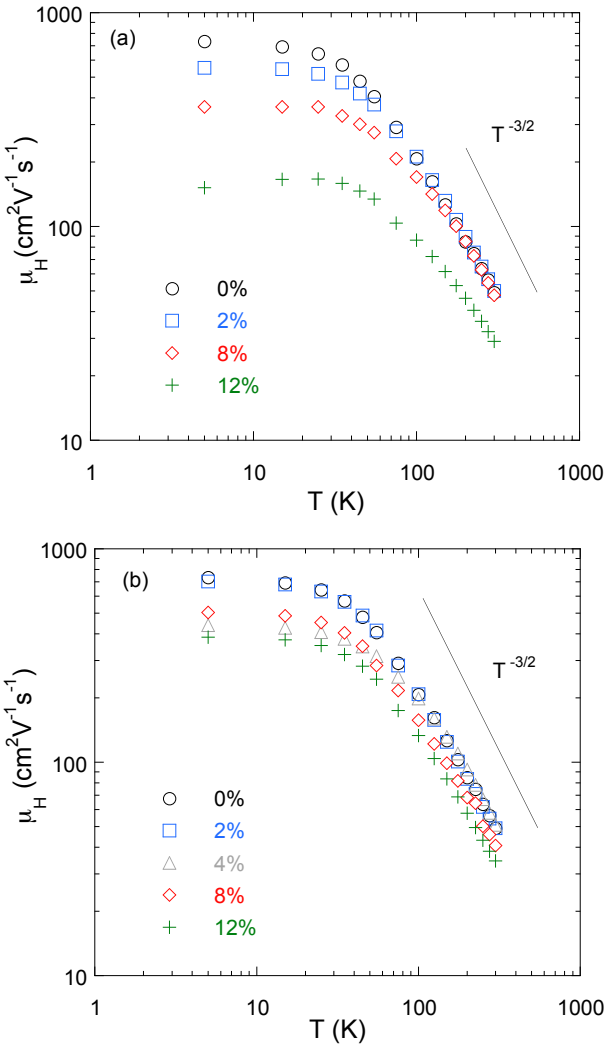
(a)
1000
100
10
1
10
100
1000
T (K)
μ_H (cm^{2}V^{-1}s^{-1})
T$^{-3/2}$
0%
2%
8%
12%
(b)
1000
100
10
1
10
100
1000
T (K)
μ_H (cm^{2}V^{-1}s^{-1})
T$^{-3/2}$
0%
2%
4%
8%
12%

Figure

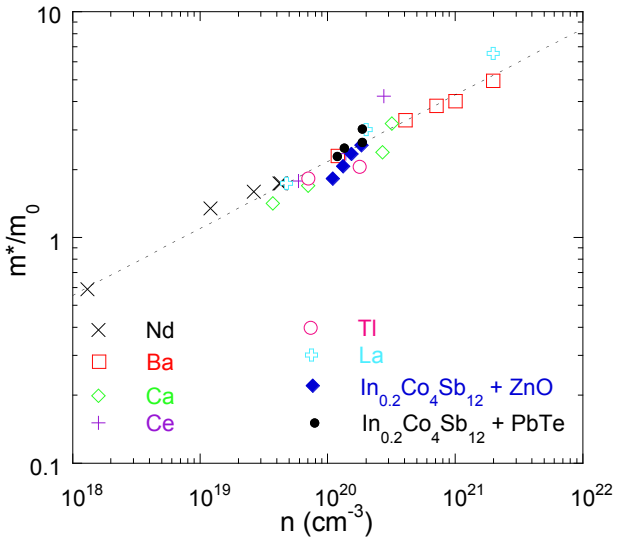
10
1
0.1
m*/m0
10^18
10^19
10^20
10^21
10^22
n (cm^-3)
Nd
Ba
Ca
Ce
Tl
La
In0.2Co4Sb12 + ZnO
In0.2Co4Sb12 + PbTe

Figure

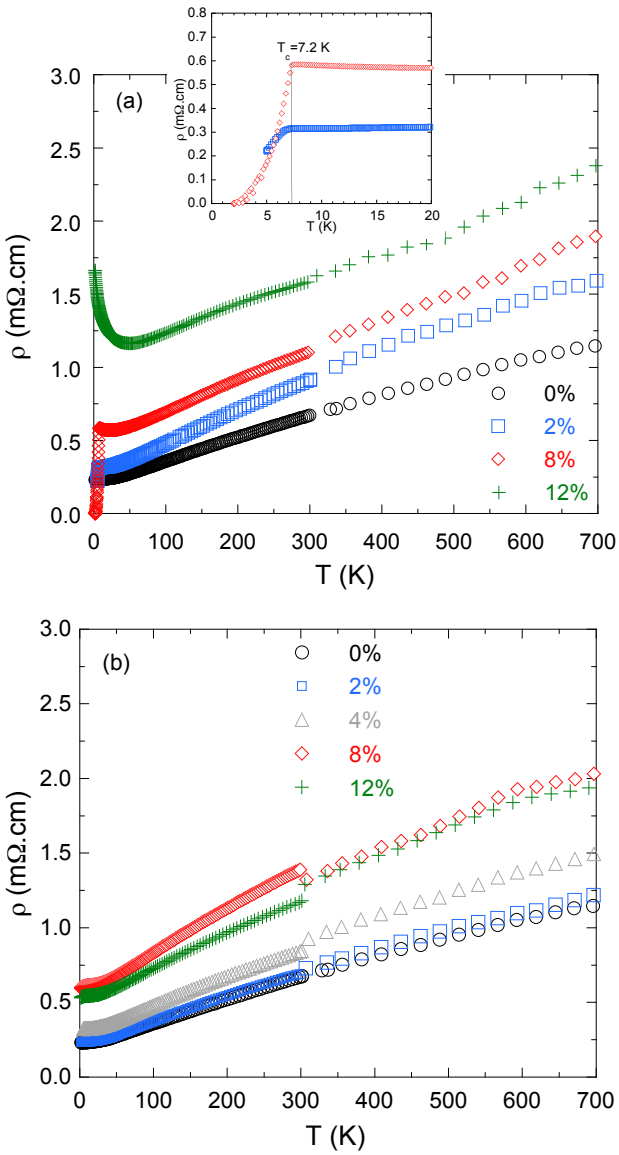

Figure

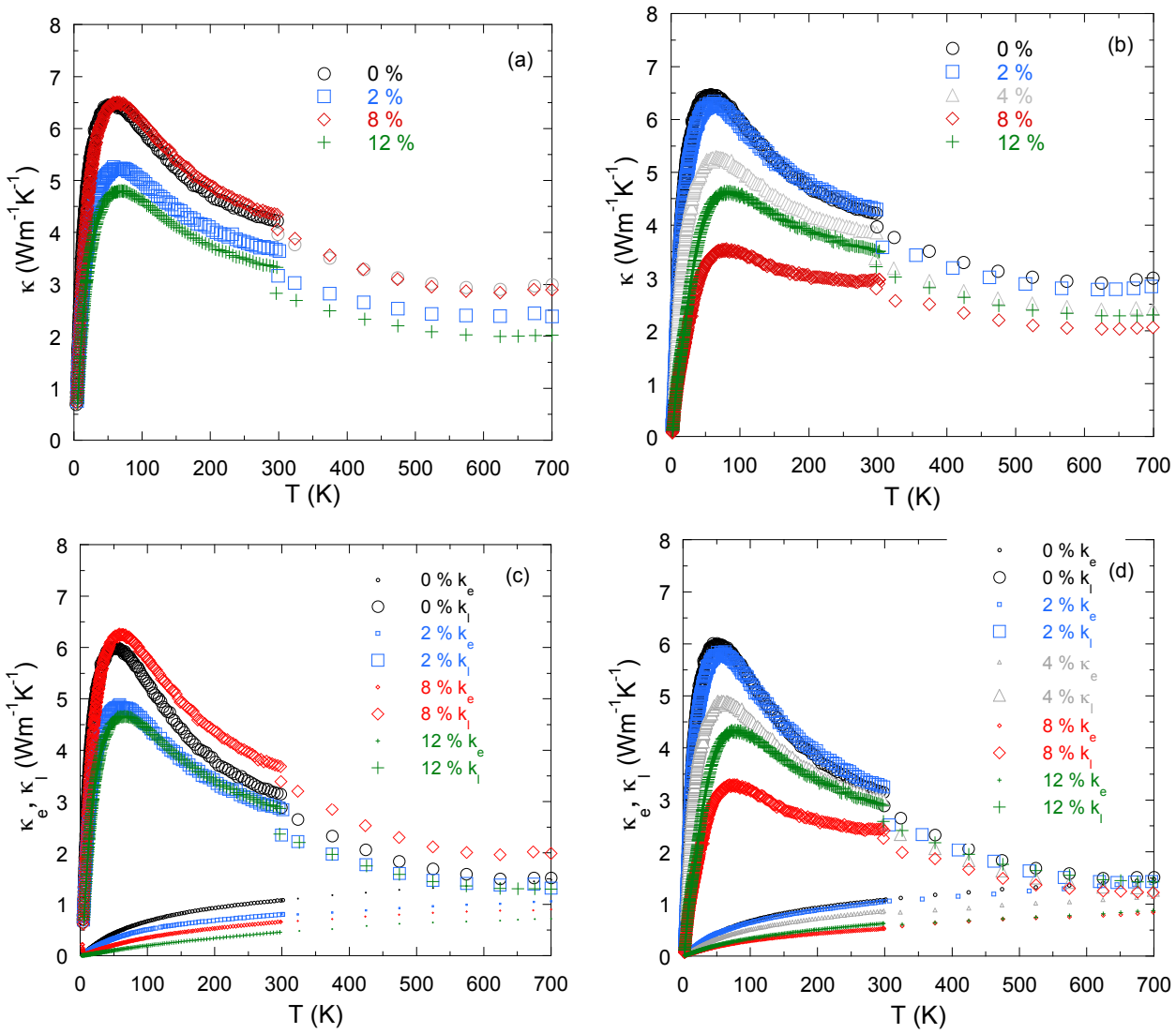
(a)
0 %
2 %
8 %
12 %
κ (Wm-1K-1)
T (K)
(b)
0 %
2 %
4 %
8 %
12 %
κ (Wm-1K-1)
T (K)
(c)
0 % ke
0 % kl
2 % ke
2 % kl
8 % ke
8 % kl
12 % ke
12 % kl
κe, κl (Wm-1K-1)
T (K)
(d)
0 % ke
0 % kl
2 % ke
2 % kl
4 % κe
4 % κl
8 % ke
8 % kl
12 % ke
12 % kl
κe, κl (Wm-1K-1)
T (K)

Figure

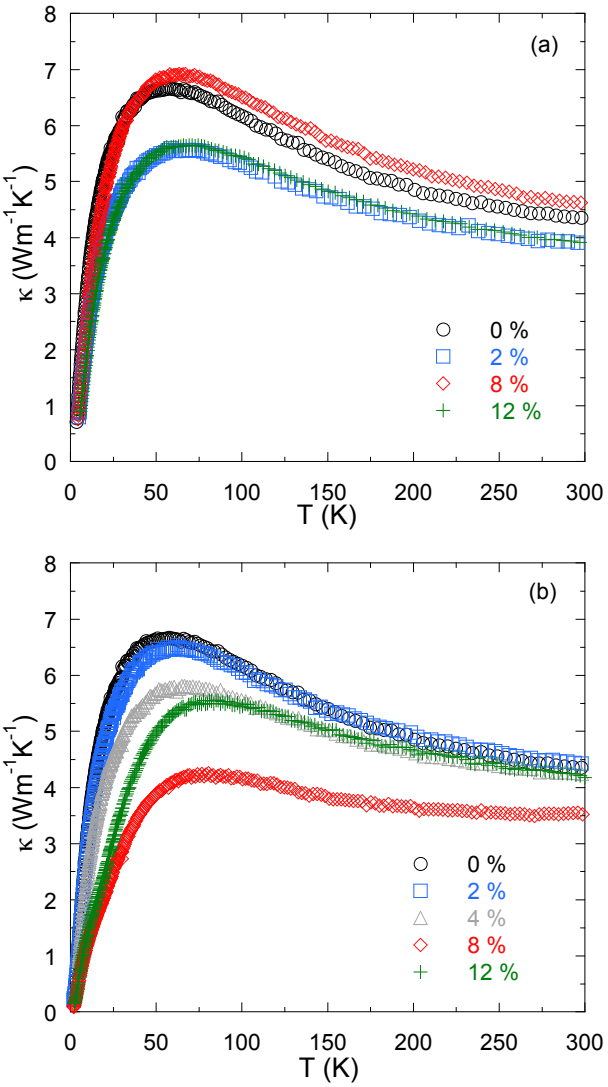

Figure